

The suppression of star formation by powerful active galactic nuclei

M.J. Page,¹ M. Symeonidis,¹ J.D. Vieira,² B. Altieri,³ A. Amblard,⁴ V. Arumugam,⁵ H. Aussel,⁶ T. Babbedge,⁷ A. Blain,⁸ J. Bock,^{2,9} A. Boselli,¹⁰ V. Buat,¹⁰ N. Castro-Rodríguez,^{11,12} A. Cava,¹³ P. Chanial,⁶ D.L. Clements,⁷ A. Conley,¹⁴ L. Conversi,³ A. Cooray,^{15,2} C.D. Dowell,^{2,9} E.N. Dubois,¹⁶ J.S. Dunlop,⁵ E. Dwek,¹⁷ S. Dye,¹⁸ S. Eales,¹⁹ D. Elbaz,⁶ D. Farrah,¹⁶ M. Fox,⁷ A. Franceschini,²⁰ W. Gear,¹⁹ J. Glenn,^{21,14} M. Griffin,¹⁹ M. Halpern,²² E. Hatziminaoglou,²³ E. Ibar,²⁴ K. Isaak,²⁵ R.J. Ivison,^{24,5} G. Lagache,²⁶ L. Levenson,^{2,9} N. Lu,^{2,27} S. Madden,⁶ B. Maffei,²⁸ G. Mainetti,²⁰ L. Marchetti,²⁰ H.T. Nguyen,^{9,2} B. O'Halloran,⁷ S.J. Oliver,¹⁶ A. Omont,²⁹ P. Panuzzo,⁶ A. Papageorgiou,¹⁹ C.P. Pearson,^{30,31} I. Pérez-Fournon,^{11,12} M. Pohlen,¹⁹ J.I. Rawlings,¹ D. Rigopoulou,^{30,32} L. Riguccini,⁶ D. Rizzo,⁷ G. Rodighiero,²⁰ I.G. Roseboom,^{16,5} M. Rowan-Robinson,⁷ M. Sánchez Portal,³ B. Schulz,^{2,27} Douglas Scott,²² N. Seymour,^{33,1} D.L. Shupe,^{2,27} A.J. Smith,¹⁶ J.A. Stevens,³⁴ M. Trichas,³⁵ K.E. Tugwell,¹ M. Vaccari,²⁰ I. Valtchanov,³ M. Viero,² L. Vigroux,²⁹ L. Wang,¹⁶ R. Ward,¹⁶ G. Wright,²⁴ C.K. Xu^{2,27} and M. Zemcov^{2,9}

- ¹Mullard Space Science Laboratory, University College London, Holmbury St. Mary, Dorking, Surrey RH5 6NT, UK
- ²California Institute of Technology, 1200 E. California Blvd., Pasadena, CA 91125, USA
- ³Herschel Science Centre, European Space Astronomy Centre, Villanueva de la Cañada, 28691 Madrid, Spain
- ⁴NASA, Ames Research Center, Moffett Field, CA 94035, USA
- ⁵Institute for Astronomy, University of Edinburgh, Royal Observatory, Blackford Hill, Edinburgh EH9 3HJ, UK
- ⁶Laboratoire AIM-Paris-Saclay, CEA/DSM/Irfu - CNRS - Université Paris Diderot, CE-Saclay, pt courrier 131, F-91191 Gif-sur-Yvette, France
- ⁷Astrophysics Group, Imperial College London, Blackett Laboratory, Prince Consort Road, London SW7 2AZ, UK
- ⁸Department of Physics & Astronomy, University of Leicester, University Road, Leicester LE1 7RH, UK
- ⁹Jet Propulsion Laboratory, 4800 Oak Grove Drive, Pasadena, CA 91109, USA
- ¹⁰Laboratoire d'Astrophysique de Marseille, OAMP, Université Aix-marseille, CNRS, 38 rue Frédéric Joliot-Curie, 13388 Marseille cedex 13, France
- ¹¹Instituto de Astrofísica de Canarias (IAC), E-38200 La Laguna, Tenerife, Spain
- ¹²Departamento de Astrofísica, Universidad de La Laguna (ULL), E-38205 La Laguna, Tenerife, Spain
- ¹³Departamento de Astrofísica, Facultad de CC. Físicas, Universidad Complutense de Madrid, E-28040 Madrid, Spain
- ¹⁴Center for Astrophysics and Space Astronomy 389-UCB, University of Colorado, Boulder, CO 80309, USA
- ¹⁵Dept. of Physics & Astronomy, University of California, Irvine, CA 92697, USA
- ¹⁶Astronomy Centre, Dept. of Physics & Astronomy, University of Sussex, Brighton BN1 9QH, UK
- ¹⁷Observational Cosmology Lab, Code 665, NASA Goddard Space Flight Center, Greenbelt, MD 20771, USA
- ¹⁸School of Physics and Astronomy, University of Nottingham, NG7 2RD, UK
- ¹⁹School of Physics and Astronomy, Cardiff University, Queens Buildings, The Parade, Cardiff CF24 3AA, UK
- ²⁰Dipartimento di Astronomia, Università di Padova, vicolo Osservatorio, 3, 35122 Padova, Italy
- ²¹Dept. of Astrophysical and Planetary Sciences, CASA 389-UCB, University of Colorado, Boulder, CO 80309, USA
- ²²Department of Physics & Astronomy, University of British Columbia, 6224 Agricultural Road, Vancouver, BC V6T 1Z1, Canada
- ²³ESO, Karl-Schwarzschild-Str. 2, 85748 Garching bei München, Germany
- ²⁴UK Astronomy Technology Centre, Royal Observatory, Blackford Hill, Edinburgh EH9 3HJ, UK
- ²⁵European Space Research and Technology Centre (ESTEC), Keplerlaan 1, 2201 AZ, Noordwijk, The Netherlands
- ²⁶Institut d'Astrophysique Spatiale (IAS), bâtiment 121, Université Paris-Sud 11 and CNRS (UMR 8617), 91405 Orsay, France
- ²⁷Infrared Processing and Analysis Center, MS 100-22, California Institute of Technology, JPL, Pasadena, CA 91125, USA
- ²⁸School of Physics and Astronomy, The University of Manchester, Alan Turing Building, Oxford Road, Manchester M13 9PL, UK
- ²⁹Institut d'Astrophysique de Paris, UMR 7095, CNRS, UPMC Univ. Paris 06, 98bis boulevard Arago, F-75014 Paris, France
- ³⁰RAL Space, Rutherford Appleton Laboratory, Chilton, Didcot, Oxfordshire OX11 0QX, UK
- ³¹Institute for Space Imaging Science, University of Lethbridge, Lethbridge, Alberta, T1K 3M4, Canada
- ³²Department of Astrophysics, Denys Wilkinson Building, University of Oxford, Keble Road, Oxford OX1 3RH, UK
- ³³CSIRO Astronomy & Space Science, PO Box 76, Epping, NSW 1710, Australia
- ³⁴Centre for Astrophysics Research, University of Hertfordshire, College Lane, Hatfield, Hertfordshire AL10 9AB, UK
- ³⁵Harvard-Smithsonian Center for Astrophysics, 60 Garden Street, Cambridge, MA 02138, USA

The old, red stars which constitute the bulges of galaxies, and the massive black holes at their centres, are the relics of a period in cosmic history when galaxies formed stars at remarkable rates and active galactic nuclei (AGN) shone brightly from accretion onto black holes. It is widely suspected, but unproven, that the tight correlation in mass of the black hole and stellar components¹ results from the AGN quenching the surrounding star formation as it approaches its peak luminosity^{2;3;4}. X-rays trace emission from AGN unambiguously⁵, while powerful star-forming galaxies are usually dust-obscured and are brightest at infrared-submillimetre wavelengths⁶. Here we report observations in the submillimetre and X-ray which show that rapid star formation was common in the host galaxies of AGN when the Universe was 2–6 Gyrs old, but that the most vigorous star formation is not observed around black holes above an X-ray luminosity of 10^{44} erg s⁻¹. This suppression of star formation in the host galaxies of powerful AGN is a key prediction of models in which the AGN drives a powerful outflow^{7;8;9}, expelling the interstellar medium of its host galaxy and transforming the galaxy’s properties in a brief period of cosmic time.

Measuring star formation in galaxies containing powerful active galactic nuclei has long been a problem, because the radiation from the AGN outshines that from star formation in almost all wavebands. Of all parts of the electromagnetic spectrum, the far-infrared to millimetre waveband offers the best opportunity to measure star formation in galaxies hosting AGN because, in contrast to strongly star-forming galaxies, AGN emit comparatively little radiation at these wavelengths¹⁰. The combination of deep X-ray and submillimetre observations therefore offers the best prospects for studying the association of star formation and accretion during the $1 < z < 3$ epoch when star formation and black hole growth in massive galaxies were at their most vigorous.

The X-ray catalogue of the *Chandra* Deep Field North (hereafter CDF-N) derives from a series of observations made with the *Chandra* X-ray observatory with a total of 2Ms exposure time¹¹. We restrict the sample to those sources detected in the most penetrating 2–8 keV band to minimize the influence of obscuration on our results, and we further limit the sample to those sources (64%) for which spectroscopic redshifts are available in the literature^{12;13}. 2–8 keV luminosities were calculated assuming that AGN X-ray spectra are power laws of the form¹⁴ $S_\nu \propto \nu^{-0.9}$; the luminosities are not corrected for absorption intrinsic to the AGN or their host galaxies. In order to restrict the X-ray sample to AGN we have discarded any sources with 2–8 keV luminosity $L_X < 10^{42}$ erg s⁻¹. SPIRE¹⁵ observations of the CDF-N were carried out in October 2009 as part of the HerMES programme¹⁶. Maps and source catalogues at 250, 350 and 500 μm were constructed¹⁷. At the depth of the SPIRE maps, the dominant source of uncertainty in the maps is confusion noise due to the high sky density of sources. For cross-matching with the *Chandra* source catalogue¹¹ we chose the 250 μm catalogue, which has the most precise positions, and we used only sources with 250 μm flux densities > 18 mJy, which corresponds to a

Region of (z,L) parameter space	Number of AGN	Number of AGN associated with 250 μm sources	Expected number of spurious associations	Fraction of AGN associated with 250 μm sources
all z , $10^{42} < L_X < 10^{45}$ erg s $^{-1}$	176	24	2.1	14 ± 3 ($^{+6}_{-5}$) %
$1 < z < 3$, $10^{43} < L_X < 10^{44}$ erg s $^{-1}$	44	11	0.5	25^{+8}_{-7} ($^{+15}_{-12}$) %
$1 < z < 3$, $10^{44} < L_X < 10^{45}$ erg s $^{-1}$	21	0	0.2	< 5 (< 13) %

Table 1: 250 μm detection statistics in the various parts of parameter space. The first row corresponds to the entire sample of secure AGN in the CDF-N, while the second and third rows correspond to the regions enclosed within the blue dashed lines in Fig. 1. Confidence intervals on the fraction of AGN associated with 250 μm sources are given at 68%, with 95% intervals enclosed in brackets. It should be noted that there is one case of two AGN being associated with the same 250 μm source. The two AGN have very similar spectroscopic redshifts, and both have X-ray luminosities between 10^{43} and 10^{44} erg s $^{-1}$. Although the two AGN cannot be resolved at 250 μm , source extraction using X-ray and 24 μm positions as priors²⁵ indicates that both AGN are 5σ sources at 250 μm .

signal/noise ratio >3 when the effects of confusion are included¹⁷. X-ray sources were matched to 250 μm sources within 6 arcseconds, corresponding to approximately 95% confidence in the 250 μm positions. The detection statistics are given in Table 1. The expected level of spurious associations between X-ray and 250 μm sources was calculated from the sky density of 250 μm sources in 10 to 30 arcsecond-radius annular regions around the X-ray source positions, and is reported in Table 1.

The distribution of CDF-N AGN in the redshift - luminosity plane is shown in Figure 1, and shows a striking trend of 250 μm detectability with X-ray luminosity: of the 24 AGN detected at 250 μm , none of them have $L_X > 10^{44}$ erg s $^{-1}$. The redshift range between 1 and 3 is of most interest, because it corresponds to the epoch in which powerful AGN accreted most of their black hole mass and present-day massive galaxies formed most of their stars. Within this redshift range, Fig. 1 shows that 11 out of 44 AGN (25^{+8}_{-7} %) with 10^{43} erg s $^{-1} < L_X < 10^{44}$ erg s $^{-1}$ are detected at 250 μm , while none of the 21 objects with $L_X > 10^{44}$ erg s $^{-1}$ are detected. The difference in detection rates has a significance of $> 99\%$ according to a single-tail Fisher's exact test. We have considered the effects that incompleteness in the spectroscopic redshifts, or absorption of the X-ray flux by gas and dust, might have on our results. We find that the systematic non-detection of the powerful AGN is robust against both effects, although X-ray absorption does appear to be a common property of the 250 μm -detected AGN. We have also verified the low 250 μm detection rate of AGN with $L_X > 10^{44}$ erg s $^{-1}$ using the Extended Chandra Deep Field South field, finding that of 49 such sources with $1 < z < 3$, only 1 is detected at 250 μm .

Infrared spectral energy distributions for the 250 μm -detected AGN were constructed by combining the SPIRE photometry with *Spitzer* 3.6 – 160 μm photometry. X-ray and infrared properties of the 11 250 μm -detected AGN with $1 < z < 3$ and L_X in the range $10^{43} - 10^{44}$ erg s $^{-1}$ are given in Table 2. In most cases the AGN contributes less than 10% to the infrared luminosity. The best-fit infrared luminosities lie between 4×10^{11} and

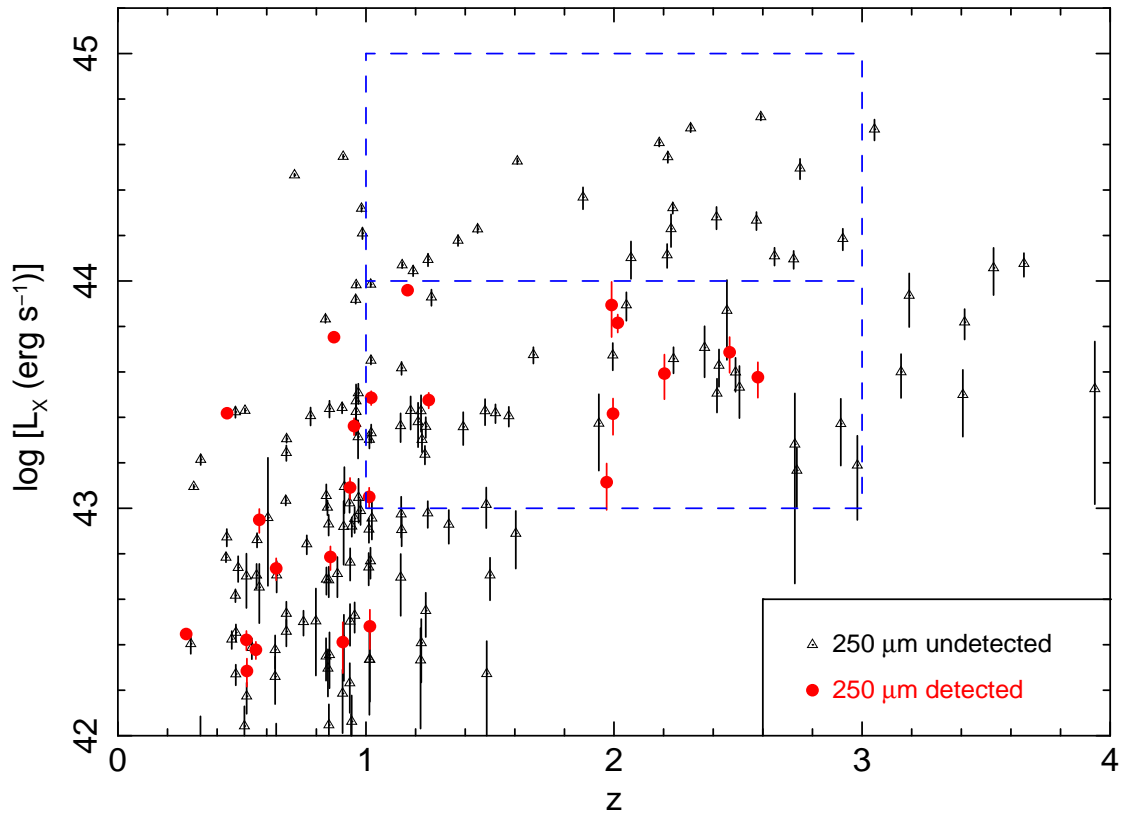


Figure 1: Redshifts and 2–8 keV X-ray luminosities of AGN in the CDF-N. The luminosities have been K-corrected assuming a spectrum $S_\nu \propto \nu^{-0.9}$ and are not corrected for intrinsic absorption. The blue dashed rectangles delimit the luminosity decades above and below 10^{44} erg s $^{-1}$ in the $1 < z < 3$ redshift range. Error bars correspond to 68% confidence.

ID	Redshift	Log L_X (erg s $^{-1}$)	Log N_H (cm $^{-2}$)	N_H corr	Log L_{IR} (L_\odot)	AGN (%)	SFR (M_\odot yr $^{-1}$)
35	2.203	43.59 $^{+0.08}_{-0.11}$	23.6 $^{+0.1}_{-0.2}$	0.15 $^{+0.05}_{-0.07}$	12.70 \pm 0.03	12	750 – 850
109	2.580	43.58 $^{+0.07}_{-0.09}$	23.4 $^{+0.1}_{-*$	0.09 $^{+0.03}_{-0.09}$	13.01 \pm 0.05	5	1660 – 1750
135	2.466	43.69 $^{+0.07}_{-0.09}$	> 24.0	> 0.30	12.81 \pm 0.05	4	1060 – 1110
158	1.013	43.05 $^{+0.04}_{-0.05}$	23.1 $^{+0.1}_{-0.1}$	0.15 $^{+0.02}_{-0.02}$	12.29 \pm 0.09	4	320 – 330
190	2.015	43.81 $^{+0.04}_{-0.04}$	23.6 $^{+0.1}_{-0.1}$	0.16 $^{+0.02}_{-0.02}$	12.88 \pm 0.03	21	1030 – 1300
331	1.253	43.48 $^{+0.03}_{-0.04}$	—	—	12.51 \pm 0.07	5	530 – 550
366	1.970	43.11 $^{+0.08}_{-0.12}$	23.4 $^{+0.1}_{-0.2}$	0.11 $^{+0.03}_{-0.04}$	12.84 \pm 0.05	3	1140 – 1170
368	1.996	43.42 $^{+0.07}_{-0.09}$	> 23.8	> 0.26	12.41 \pm 0.06	3	420 – 430
384	1.021	43.49 $^{+0.03}_{-0.03}$	23.4 $^{+0.1}_{-0.1}$	0.25 $^{+0.02}_{-0.03}$	11.55 \pm 0.17	11	50 – 60
455	1.168	43.96 $^{+0.02}_{-0.02}$	—	—	11.97 \pm 0.04	30	110 – 160
500	1.990	43.89 $^{+0.10}_{-0.14}$	23.2 $^{+0.2}_{-*$	0.07 $^{+0.03}_{-0.07}$	12.62 \pm 0.03	4	690 – 710

Table 2: Properties of SPIRE-detected AGN. Data are given for AGN with $1 < z < 3$ and 10^{43} erg s $^{-1} < L_X < 10^{44}$ erg s $^{-1}$. The first column gives the ID number of the source in the X-ray catalogue¹¹. The second column gives the redshift, and the third column gives the logarithm of the 2–8 keV X-ray luminosity. The fourth column gives the log of the column density of absorbing gas (units of hydrogen atoms per cm 2) implied by the ratio of 2–8 keV to 0.5–2 keV X-rays; a dash indicates no evidence for photoelectric absorption in X-rays, and an asterix is used where the lower limit to the column density is unconstrained. The fifth column gives the correction to log L_X to account for the absorption. The sixth column gives the 8–1000 μ m IR luminosity. The seventh column gives the maximum likely contribution of an AGN to the infrared luminosity, and the eighth column gives the range of star formation rate implied by the infrared luminosity, where the upper and lower limits correspond to zero AGN contribution and the maximum AGN contribution to the IR luminosity, respectively. Photometry for the spectral energy distributions was extracted from *Spitzer* and SPIRE images using the X-ray and 24 μ m catalogue positions as priors²⁵. Total 8–1000 μ m infrared luminosities were then determined by fitting templates²⁶ to the spectral energy distributions²⁷. Upper limits to the AGN contribution to the infrared luminosities were obtained by normalising an AGN template in the mid infrared²⁸.

$10^{13} L_\odot$, implying star formation rates between 50 and 1750 M_\odot per year¹⁸.

We performed a stacking analysis for the $1 < z < 3$ AGN to probe below the confusion limit of the SPIRE images. We split the sample into five bins of L_X from 10^{43} to 10^{45} erg s $^{-1}$ and determined the average star formation rates of AGN in each bin. The results are shown in Figure 2. In the redshift range $1 < z < 3$, the mean star formation rate in AGN with L_X of $10^{43} - 10^{44}$ erg s $^{-1}$ is $214 \pm 25 M_\odot$ per year, compared to a mean star formation rate for AGN with $L_X > 10^{44}$ erg s $^{-1}$ of $65 \pm 18 M_\odot$ per year. These averages are independent of the SPIRE 250 μ m detection limit because they are obtained from a stack of all sources within a given range of L_X , whether detected at 250 μ m or not.

At redshifts of 1–3, the X-ray luminosity of 10^{44} erg s $^{-1}$, which divides the regions of 250 μ m detection and non-detection in Fig. 1, corresponds approximately to the knee in the luminosity function of AGN¹⁹. The steep shape of the luminosity function at $L_X > 10^{44}$ erg s $^{-1}$ implies that this part of the luminosity function is dominated by objects which are at the peak of their accretion rates. Our observations therefore imply that the most prodigious episodes of star formation are common in the host galaxies of $1 < z < 3$ AGN, but avoid powerful AGN in which accretion is at its peak.

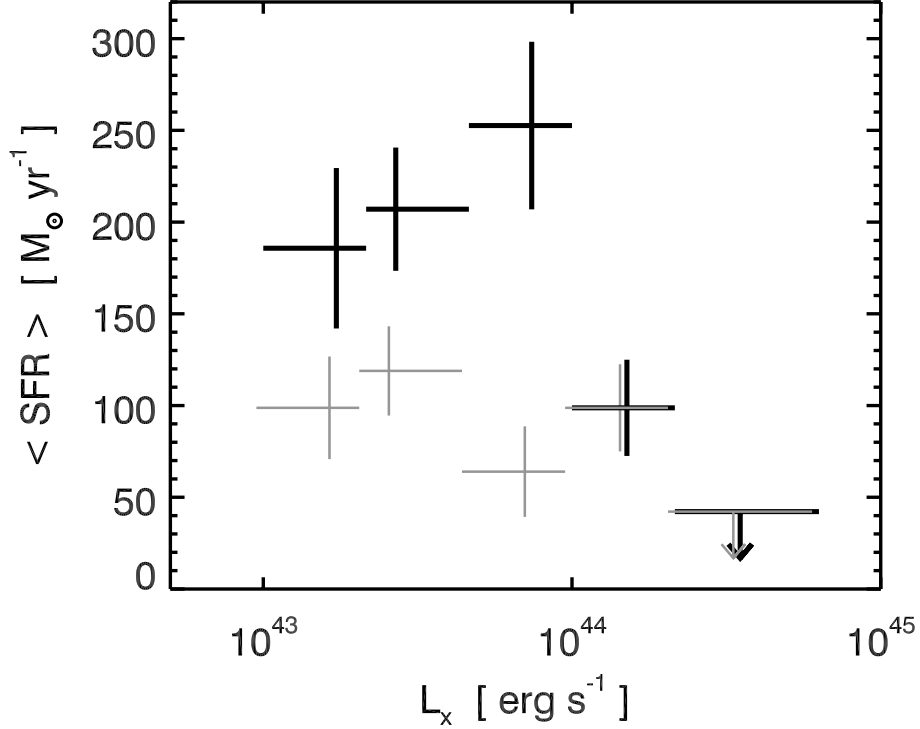


Figure 2: Star formation rates derived from averaged far-IR luminosities of $1 < z < 3$ AGN. We converted the 250, 350 and 500 μm flux densities for each source into an equivalent 8-1000 μm luminosity by fitting a grey-body curve, with a temperature of 30 K in the rest-frame of the source, an emissivity index of $\beta = 1.6$, and a power-law extension to the Wien side²⁹ and multiplying by $4\pi D_L^2$ where D_L is the luminosity distance. Fluctuations in the map sometimes scatter the fluxes of undetected sources to negative values, which translate to negative luminosities when multiplied by $4\pi D_L^2$. Such negative solutions for individual AGN were allowed so as not to produce an artificial positive bias in the averages. The luminosities were averaged in 5 bins in L_X , which were chosen to include a similar number of AGN in each bin. The average luminosities were then converted to star formation rates¹⁸. AGN which are individually detected at 250 μm are included in the averages shown in bold black, but have been excluded from the averages which are shown in grey, to show the contribution that these sources make to the average star formation rates. The grey points have been offset horizontally from the bold black points for clarity. Error bars correspond to 68% confidence and were determined by bootstrap resampling, with a 7% systematic error added in quadrature to account for the calibration error on SPIRE photometry.

This systematic non-coincidence of the peak periods of star formation and accretion implies a palpable interaction between the two processes, and provides a powerful discriminator for the form of AGN feedback which is responsible for terminating star formation in the host galaxy. Two families of feedback models have been proposed, widely referred to as ‘quasar mode’ and ‘radio mode’²⁰. In quasar-mode feedback, a luminous AGN generates a powerful wind which terminates star formation by driving the interstellar medium from the surrounding host galaxy. In radio-mode feedback, star formation is suppressed because collimated jets of relativistic particles emitted by a radiatively-inefficient AGN prevent gas in the surrounding hot halo from cooling, thereby starving the galaxy of cool gas from which to form stars.

Radio-mode feedback is commonly invoked in semi-analytical models to limit galaxy masses and luminosities^{21;20}. In these models, black holes grow through luminous accretion episodes and black hole mergers. The correlation between black hole and bulge mass comes from assuming that a fixed fraction of the gas is accreted by the nucleus during each star forming episode that results from a galaxy merger or disc instability, and hence star formation and accretion rate should be correlated over the full range of luminosity. Our observations are therefore inconsistent with models in which AGN influence their host galaxies only through radio mode feedback^{21;20}. In contrast, models of galaxy formation in which quasar-mode feedback is responsible for terminating the star formation^{22;8;7;9}, and which have received some observational support recently^{23;24}, predict that the AGN luminosity peaks later than the star formation rate, and thus are consistent with our observations. These models also predict that residual star formation, at the level of a few tens of per cent of the peak, will continue during the period in which the AGN luminosity is at its maximum, consistent with our stacked results which show that on average AGN with $L_X > 10^{44}$ erg s⁻¹ are still forming stars at approximately 65 M_⊙ per year. Our observations do not discriminate between models invoking major mergers⁸ or accretion of gas into a massive halo²² as the trigger for the intense star formation. After the interstellar medium has been driven out by the luminous AGN and the AGN itself becomes starved of fuel, radio-mode feedback is the most credible agent by which further star formation is inhibited.

References

- [1] Häring & Rix, On the Black Hole Mass-Bulge Mass Relation. *Astrophys. J.*, 604, L89-L92 (2004)
- [2] Silk J. & Rees M.J., Quasars and galaxy formation. *Astron. Astrophys.*, 331, L1-L4 (1998)
- [3] Fabian, A.C., The obscured growth of massive black holes. *Mon. Not. R. Astron. Soc.*, 308, L39-L43 (1999)
- [4] King, A.R., Black hole outflows. *Mon. Not. R. Astron. Soc.*, 402, 1516-1522 (2010)

- [5] Brandt W.N. & Hasinger G., Deep Extragalactic X-Ray Surveys. *Annu. Rev. Astron. Astrophys.*, 43, 827-859 (2005)
- [6] Sanders D.B. & Mirabel I.F., Luminous Infrared Galaxies. *Annu. Rev. Astron. Astrophys.*, 34, 749-792 (1996)
- [7] Di Matteo T., Springel V. & Hernquist L., Energy input from quasars regulates the growth and activity of black holes and their host galaxies. *Nature*, 433, 604-607 (2005)
- [8] Springel V., Di Matteo T., & Hernquist L., Modelling feedback from stars and black holes in galaxy mergers. *Mon. Not. R. Astron. Soc.*, 361, 776-794 (2005)
- [9] Sijacki D., Springel V., Di Matteo T., Hernquist L., A unified model for AGN feedback in cosmological simulations of structure formation. *Mon. Not. R. Astron. Soc.*, 380, 877-900 (2007)
- [10] Hatziminaoglou, E., et al., HerMES: Far infrared properties of known AGN in the HerMES fields. *Astron. Astrophys.*, 518, L33 (2010)
- [11] Alexander D.M., Bauer F.E., Brandt W.N., et al., The Chandra Deep Field North Survey. XIII. 2 Ms Point-Source Catalogs. *Astron. J.*, 126, 539-574 (2003)
- [12] Trouille L., Barger A.J., Cowie L.L., Yang Y., Mushotzky R.F., The OPTX Project. I. The Flux and Redshift Catalogs for the CLANS, CLASXS, and CDF-N Fields. *Astrophys. J. Suppl.*, 179: 1-18 (2008)
- [13] Barger A.J., et al., A Highly Complete Spectroscopic Survey of the GOODS-N Field. *Astrophys. J.*, 689, 687-708 (2008)
- [14] Mateos S., Barcons X., Carrera F.J., Ceballos M.T., Hasinger G., Lehmann I., Fabian A.C., Streblyanska A., XMM-Newton observations of the Lockman Hole IV: spectra of the brightest AGN. *Astron. Astrophys.*, 444, 79-99 (2005)
- [15] Griffin M.J., et al., The Herschel-SPIRE instrument and its in-flight performance. *Astron. Astrophys.*, 518, L3 (2010)
- [16] Oliver, S.J., et al., HerMES: SPIRE galaxy number counts at 250, 350, and 500 μm . *Astron. Astrophys.*, 518, L21 (2010)
- [17] Smith A.J., et al., HerMES: point source catalogues from deep Herschel-SPIRE observations. *Mon. Not. R. Astron. Soc.*, 419, 377-389 (2012)
- [18] Kennicutt, R.C., The global Schmidt law in star-forming Galaxies. *Astrophys. J.*, 498, 541-552 (1998)

- [19] Ebrero J., et al., The XMM-Newton serendipitous survey. VI. The X-ray luminosity function. *Astron. Astrophys.*, 493, 55-69 (2009)
- [20] Croton D.J., et al., The many lives of active galactic nuclei: cooling flows, black holes and the luminosities and colours of galaxies. *Mon. Not. R. Astron. Soc.*, 365, 11-28 (2006)
- [21] Bower R. G., et al., Breaking the hierarchy of galaxy formation. *Mon. Not. R. Astron. Soc.*, 370, 645-655 (2006)
- [22] Granato G.L., et al., A physical model for the coevolution of QSOs and their spheroidal hosts. *Astrophys. J.*, 600, 580-594 (2004)
- [23] Farrah D., et al., Direct evidence for termination of obscured star formation by radiatively driven outflows in reddened QSOs. *Astrophys. J.*, 745, 178 (2012)
- [24] Cano-Díaz M., Maiolino R., Marconi A., Netzer H., Shemmer O., Cresci G., Observational evidence of quasar feedback quenching star formation at high redshift. *Astron. Astrophys.*, 537, L8 (2012)
- [25] Roseboom I.G., et al., The Herschel Multi-Tiered Extragalactic Survey: source extraction and cross-identifications in confusion-dominated SPIRE images. *Mon. Not. R. Astron. Soc.*, 409, 48-65 (2010)
- [26] Siebenmorgen R. & Krügel E., Dust in starburst nuclei and ULIRGs. SED models for observers. *Astron. Astrophys.*, 461, 445-453 (2007)
- [27] Symeonidis M., et al., The link between SCUBA and Spitzer: cold galaxies at $z \leq 1$. *Mon. Not. R. Astron. Soc.*, 397, 1728-1738 (2009)
- [28] Seymour, N., et al., HerMES: SPIRE emission from radio-selected active galactic nuclei. *Mon. Not. R. Astron. Soc.*, 413, 1777-1786 (2011)
- [29] Blain, A.W., Barnard V.E. & Chapman S.C., Submillimetre and far-infrared spectral energy distributions of galaxies: the luminosity-temperature relation and consequences for photometric redshifts. *Mon. Not. R. Astron. Soc.*, 338, 733-744 (2003)

Supplementary Information is linked to the online version of the paper at www.nature.com/nature

Acknowledgments SPIRE has been developed by a consortium of institutes led by Cardiff Univ. (UK) and including Univ. Lethbridge (Canada); NAOC (China); CEA, LAM (France); IFSI, Univ. Padua (Italy); IAC (Spain); Stockholm Observatory (Sweden); Imperial College London, RAL, UCL-MSSL, UKATC, Univ. Sussex

(UK); Caltech, JPL, NHSC, Univ. Colorado (USA). This development has been supported by national funding agencies: CSA (Canada); NAOC (China); CEA, CNES, CNRS (France); ASI (Italy); MCINN (Spain); SNSB (Sweden); STFC, UKSA (UK); and NASA (USA).

Author Contributions This paper represents the combined work of the HerMES collaboration, the SPIRE Instrument Team's extragalactic survey. M. Page planned the study, and wrote the draft version of the paper. M. Symeonidis fitted models to the spectral energy distributions of the sources and J.D. Vieira performed the stacking analysis. All other coauthors of this paper contributed extensively and equally by their varied contributions to the SPIRE instrument, Herschel mission, analysis of SPIRE and HerMES data, planning of HerMES observations and scientific support of HerMES, and by commenting on this manuscript as part of an internal review process.

Author Information Reprints and permissions information is available at www.nature.com/reprints. The authors declare that they have no competing financial interests. Correspondence and requests for materials should be addressed to M.Page (mjp@mssl.ucl.ac.uk).

Supplementary Information

Spectroscopic redshifts of CDF-N X-ray sources

We have taken a recent compilation¹³ as our main source of spectroscopic redshifts. These redshifts are given to two decimal places, but the majority of them originate from earlier studies, so we have in most cases obtained more precise redshifts by tracing them back to the original publications. Where there is a significant discrepancy ($> 2\%$) between a spectroscopic redshift in our main source and that given in earlier literature, we have adopted the redshift from our main source¹³. We have utilised a number of spectroscopic redshifts which are not listed there. The redshifts and literature references for these cases are given in Table S1.

Effect of redshift incompleteness

While we have restricted our study to objects within the CDF-N which have optical spectroscopic identifications and redshifts to ensure fidelity in redshifts and luminosities, we must examine whether the limited spectroscopic completeness (64%) has any effect on our results. A large fraction of the X-ray sources within the CDF-N have photometric redshifts (i.e. redshifts estimated by comparing photometry in a number of bands to that expected from galaxy template spectra as a function of redshift) in the same compilation that we use for our spectroscopic redshifts¹³. Although these photometric redshifts are of low accuracy and reliability compared to the spectroscopic redshifts, they raise the redshift completeness of the 2–8 keV X-ray sources to 87%, and so offer a good test as to whether the spectroscopic completeness has a significant influence on our results. Table S2 gives statistics equivalent to those shown in Table 1 of the main paper, but with the photometric redshifts included. As found for the spectroscopic-only sample, no AGN more luminous than 10^{44} erg s^{-1} are associated with 250 μm sources.

We can be further reassured that our main result is not affected by the spectroscopic incompleteness by looking specifically at the identification statistics of those 2–8 keV X-ray sources which are associated with 250 μm sources. A total of 33 2–8 keV X-ray sources are associated with 250 μm sources, of which 27 are spectroscopically identified. The spectroscopically-identified fraction of these sources is thus 82%, higher than the 2–8 keV source population as a whole. For the 6 sources without spectroscopic redshifts, Fig. S1 shows the tracks of X-ray luminosity as a function of redshift. We can see that with respect to the $1 < z < 3$, 10^{43} erg $s^{-1} < L_X < 10^{45}$ erg s^{-1} region which is well sampled by the X-ray and submillimetre surveys, sources 31, 37 and 431 from the X-ray catalogue¹² have $L_X < 10^{44}$ erg s^{-1} for all $1 < z < 3$. The tracks for sources 107, 221 and 406 all cross the upper rectangle corresponding to $1 < z < 3$, 10^{44} erg $s^{-1} < L_X < 10^{45}$ erg s^{-1} , and so should be examined in more detail. The track for source 221 only enters this rectangle for a tiny redshift interval ($2.94 < z < 3.0$). Although our main redshift compilation¹³ does not give a photometric redshift for source

Source number in X-ray catalogue ¹²	Spectroscopic redshift	Reference
91	0.294	30
121	0.520	31
152	0.540	14
191	0.952	14
196	0.680	32
205	0.943	14
220	4.420	33
223	2.724	34
243	0.557	35
266	1.2258	14
287	2.737	14
292	0.497	36
317	1.760	14
342	0.518	30
377	3.1569	14
412	1.1435	14
423	2.365	14
441	0.634	31
443	0.033	30
470	0.231	31

Table S1: Spectroscopic redshifts which do not come from our main source¹³ and references to the literature in which these redshifts are published.

221, a photometric redshift of 1.9 is found elsewhere in the literature³⁷, in which case it has $L_X < 10^{44}$ erg s⁻¹ in keeping with the other 250 μ m-detected AGN. Source 107 is within 6 arcsec of the same 250 μ m source as a brighter X-ray source (source 109), which has a spectroscopic redshift of 2.58. The brighter X-ray source is closer to the 250 μ m source position than source 107, and source extraction using X-ray and 24 μ m positions as priors²⁵ does not recover significant 250 μ m emission for source 107, leaving some doubt about the reality of the association. Source 107 has a photometric redshift of 1.15, but could be physically associated with source 109 at $z = 2.58$ given that they are only separated by 2.7 arcsec. It can be seen from Fig. S1 that whichever of the two redshifts is adopted for source 107, it has L_X between 10^{43} erg s⁻¹ and 10^{44} erg s⁻¹, and hence if the association of source 107 and the 250 μ m source is real, it too has $L_X < 10^{44}$ erg s⁻¹, in keeping with the other 250 μ m-detected AGN. Finally, we come to source 406, which is the brightest of the six X-ray sources. From the track in Fig. S1, it appears the most likely of the six to be found within the $1 < z < 3$, 10^{44} erg s⁻¹ $< L_X < 10^{45}$ erg s⁻¹ region of our survey. This source is extremely faint in the optical, with an R -band magnitude of 27.8³¹, and there are no estimates of photometric redshift available in the literature. The association of this X-ray source with the 250 μ m source must be regarded with some doubt, however, because it is located just 5.5 arcsec to the south of a brighter 24 μ m and radio source which is closer to the 250 μ m position. Source extraction using

Region of (z,L) parameter space	Number of AGN	Number of AGN associated with 250 μm sources	Expected number of spurious associations	Fraction of AGN associated with 250 μm sources
all z , $10^{42} < L_X < 10^{45} \text{ erg s}^{-1}$	248	27	2.8	11 ± 2 (± 4) %
$1 < z < 3$, $10^{43} < L_X < 10^{44} \text{ erg s}^{-1}$	61	12	0.7	20 ± 6 ($^{+12}_{-9}$) %
$1 < z < 3$, $10^{44} < L_X < 10^{45} \text{ erg s}^{-1}$	25	0	0.3	< 4 (< 11) %

Table S2: 250 μm detection statistics in the various parts of parameter space when AGN with photometric redshifts are included as well as those with spectroscopic redshifts. The first row corresponds to the full AGN luminosity and redshift parameter space in the CDF-N, while the second and third rows correspond to the regions enclosed within the blue dashed lines in Fig. 1.

X-ray and 24 μm positions as priors²⁵ detects source 406 only at the 3σ level. Nonetheless, this source does represent the single example of an X-ray source, potentially associated with a 250 μm source, with a reasonable likelihood of lying within the $1 < z < 3$, $L_X > 10^{44} \text{ erg s}^{-1}$ region. Equally, it may fall within the $1 < z < 3$, $L_X < 10^{44} \text{ erg s}^{-1}$ region. To summarise, it appears that the sources without spectroscopic redshifts are likely to harbour at most one object within the redshift range $1 < z < 3$, which has $L_X > 10^{44} \text{ erg s}^{-1}$.

Effect of X-ray absorption

X-rays in the 2–8 keV band can penetrate considerable column densities of material, but column densities $> 10^{23} \text{ cm}^{-2}$ can lead to significant attenuation of the X-ray flux. Conceivably, the different 250 μm detection rates for AGN above and below $10^{44} \text{ erg s}^{-1}$ could be a consequence of X-ray absorption, if 250 μm -luminous AGN are systematically more heavily absorbed than AGN which are not detected at 250 μm . X-rays in the 0.5–2 keV band are absorbed more easily than those in the 2–8 keV band which was used to select our X-ray sample, and hence the hardness ratio of 2–8 keV / 0.5–2 keV X-rays is a crude but effective estimator of the degree of X-ray absorption.

For each 2–8 keV X-ray source, we used the Portable Interactive Multi-Mission Simulator (PIMMS; <http://heasarc.nasa.gov/docs/software/tools/pimms.html>) to convert from hardness ratios to spectral indices and column densities. The intrinsic spectra of faint AGN without absorption are power laws of the form $S_\nu \propto \nu^{-\alpha}$ with a mean $\alpha = 0.9$, and an rms scatter in α of 0.2^{15} . We took a hardness ratio corresponding to $\alpha = 0.5$ (2σ from the mean) as the threshold beyond which we considered sources as absorbed. For absorbed sources, we used PIMMS to estimate the column density, assuming an intrinsic spectral index $\alpha = 0.9$. PIMMS was then used to calculate the expected degree of attenuation to the observed 2–8 keV X-rays from the column density estimate. The X-ray luminosities were then adjusted accordingly. Where only a lower limit to the hardness ratio is available (due to the faintness of the object in the 0.5–2 keV X-ray band), the luminosity correction corresponding to the lower limit is applied.

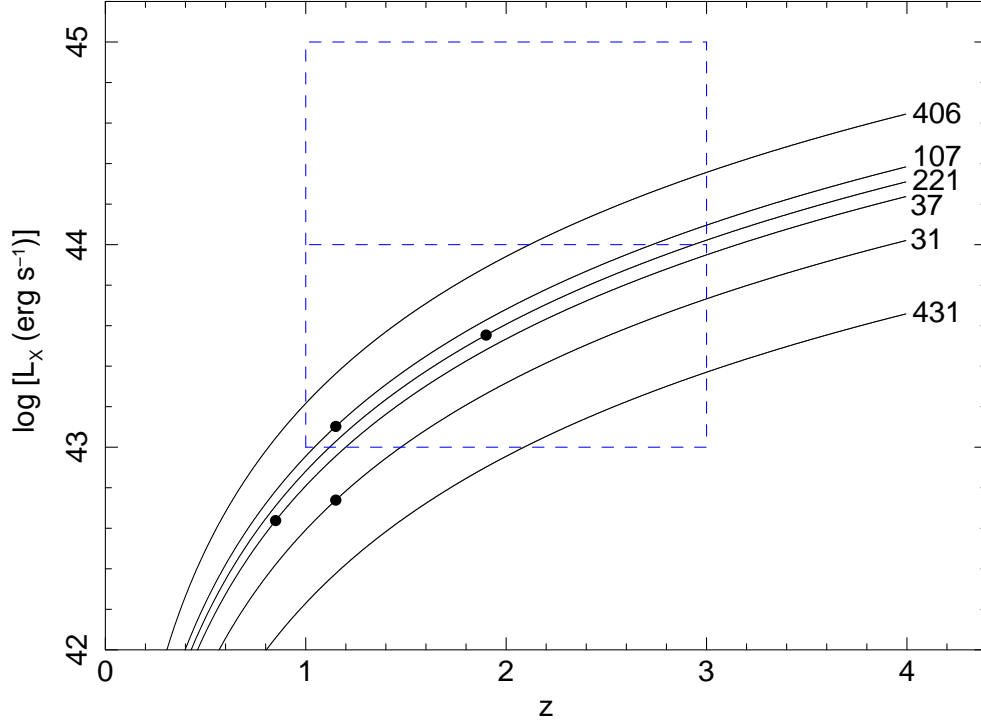


Figure S1: 2–8 keV X-ray luminosities as a function of redshift for 2–8 keV X-ray sources which are associated with $250\ \mu\text{m}$ sources and which do not have spectroscopic redshifts. The bold dots indicate photometric redshifts, where available. The blue dashed rectangle delimits the luminosity decades above and below $10^{44}\ \text{erg s}^{-1}$ in the $1 < z < 3$ redshift range as in Fig. 1. Error bars correspond to 68% confidence.

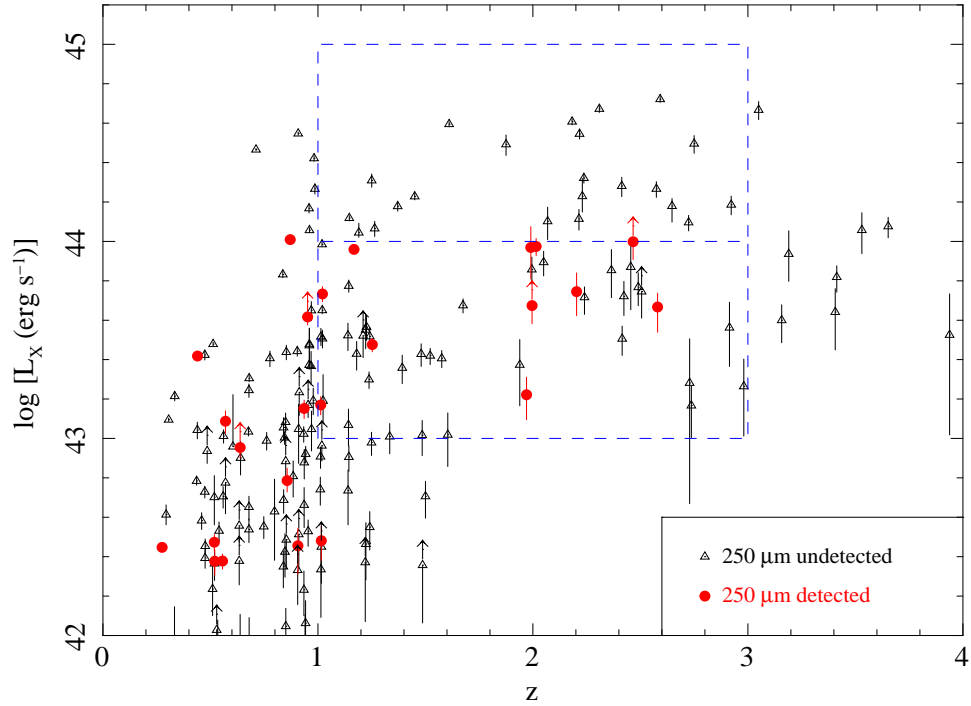


Figure S2: 2–8 keV X-ray luminosities as a function of redshift after correction for absorption. AGN with lower-limit hardness ratios have absorption-corrected luminosities with unconstrained upper bounds, and these are shown as upward pointing arrows. The blue dashed rectangle delimits the luminosity decades above and below $10^{44}\ \text{erg s}^{-1}$ in the $1 < z < 3$ redshift range as in Fig. 1. Error bars correspond to 68% confidence.

Fig. S2 shows how Fig. 1 would be affected by the absorption corrections. More than half of the 250 μm -detected AGN increase in luminosity when the absorption corrections are applied, but on the whole these corrections are quite modest, with the majority amounting to less than 40% change in luminosity. None of the 250 μm -detected AGN move into the $1 < z < 3$, $10^{44} \text{ erg s}^{-1} < L_X < 10^{45} \text{ erg s}^{-1}$ region. Although several of the 250 μm -detected AGN move close to the $10^{44} \text{ erg s}^{-1}$ boundary, and the absorption corrections for two of the 250 μm -detected AGN are lower limits such that they may have intrinsic luminosities $> 10^{44} \text{ erg s}^{-1}$, the essential characteristic of Fig. 1, the low 250 μm detection rate above $10^{44} \text{ erg s}^{-1}$, persists.

The fraction of absorbed AGN is known to depend on luminosity³⁸ such that absorption is less common in the most luminous AGN. In light of this interdependency between luminosity and absorption, we have also examined the 250 μm detection rate of AGN with $1 < z < 3$ and $10^{43} \text{ erg s}^{-1} < L_X < 10^{45} \text{ erg s}^{-1}$ as a function of X-ray absorption rather than X-ray luminosity. Dividing the sample into absorbed and unabsorbed sources using the hardness-ratio criterion given above, we have 9 absorbed and 2 unabsorbed AGN detected at 250 μm , and 27 each of absorbed and unabsorbed sources which are not detected at 250 μm . Applying a Fisher's exact test, we find that the difference in 250 μm detection rate between absorbed and unabsorbed sources is significant at a little less than 95%. We can reduce the influence of the intrinsic anti-correlation between absorption and luminosity within the sample under test by excluding the sources with X-ray luminosities above $10^{44} \text{ erg s}^{-1}$. We then have 9 absorbed and 2 unabsorbed sources detected at 250 μm , with 19 absorbed and 14 unabsorbed sources undetected at 250 μm . Applying the Fisher's test, the statistical significance at which the 250 μm detection rate depends on X-ray absorption drops to 90%. Hence, whereas we can demonstrate that the 250 μm detection rate depends on X-ray luminosity, we can not state with such confidence that the 250 μm detection rate depends on X-ray absorption.

Verification in the Extended Chandra Deep Field South

We have verified that the main result of this work, the paucity of 250 μm -detections amongst X-ray-luminous AGN, is reproduced in the Extended Chandra Deep Field South (ECDF-S), which is a larger field than the CDF-N, containing a larger sample of AGN with $L_X > 10^{44} \text{ erg s}^{-1}$. We used the published X-ray catalogue³⁹ and spectroscopic redshifts⁴⁰. The SPIRE observations of the ECDF-S are shallower than those of CDF-N, but nonetheless are limited primarily by confusion. As with CDF-N, we have adopted a detection threshold of 18 mJy at 250 μm , and cross-correlated the X-ray and submillimetre catalogues with a matching radius of 6 arcseconds. The 250 μm detections in the ECDF-S (z, L) plane are shown in Figure S3, analogous to Fig. 1 of the main article. Of 49 sources with $1 < z < 3$ and $L_X > 10^{44} \text{ erg s}^{-1}$, only 1 is detected at 250 μm , confirming the low detection rate obtained in the CDF-N.

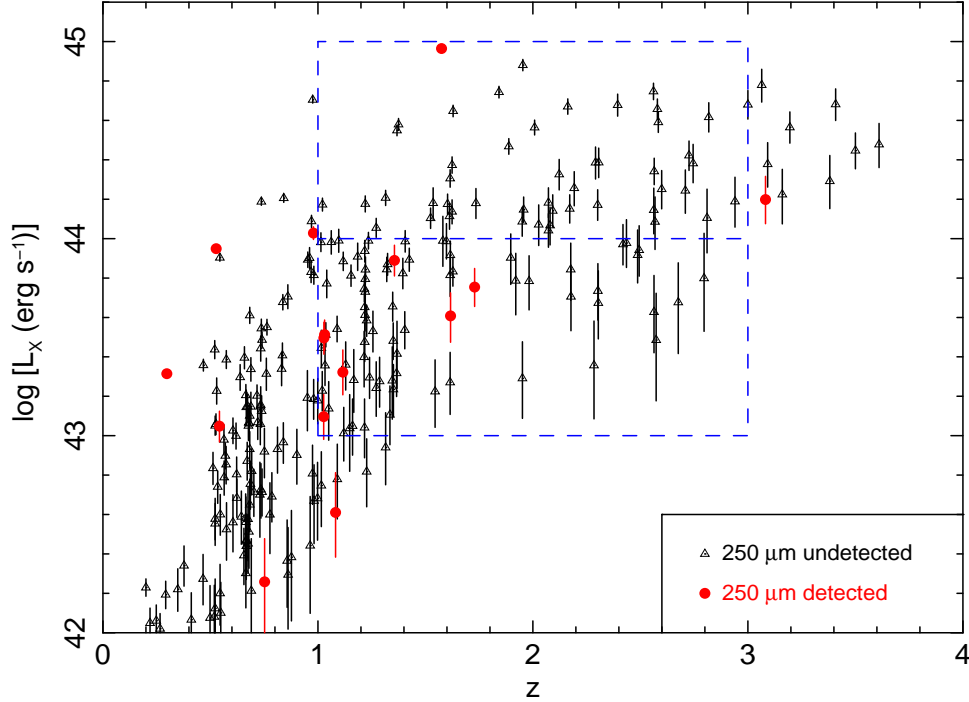


Figure S3: 2–8 keV X-ray luminosities as a function of redshift for the ECDF-S field. The blue dashed rectangle delimits the luminosity decades above and below 10^{44} erg s^{-1} in the $1 < z < 3$ redshift range as in Fig. 1. Error bars correspond to 68% confidence.

Infrared spectral energy distributions of 250 μm -detected AGN

The spectral energy distributions and best fit models for the AGN associated with 250 μm sources with $1 < z < 3$ and 10^{43} erg $s^{-1} < L_X < 10^{44}$ erg s^{-1} , are shown in Fig. S4

Obtaining the average star formation rates through stacking

The average star formation rates shown in Fig. 2 were obtained by averaging the far-infrared luminosities of the AGN to account for the different redshifts of the different AGN. It is more common in stacking analyses to average the fluxes of the objects, and then to use the average flux and the median redshift of the sample to infer an average luminosity. Here we examine how the results would change if we used this latter method rather than stacking directly in luminosity. Fig. S5 shows the star formation rates obtained by the two different methods. The two methods give consistent results, and in both cases the average star formation rates are significantly higher for AGN with $\log L_X < 10^{44}$ erg s^{-1} than for AGN with $\log L_X > 10^{44}$ erg s^{-1} . We have also examined how the star formation rates would differ if only one of the SPIRE bands were used, instead of all three, to determine the luminosities. For each of the SPIRE bands, we derived a luminosity for each source by normalising a 30 K grey-body in the rest frame to the SPIRE flux and multiplying by $4\pi D_L^2$, before averaging the luminosities in each bin. The star formation rates so derived from the three SPIRE bands are shown in

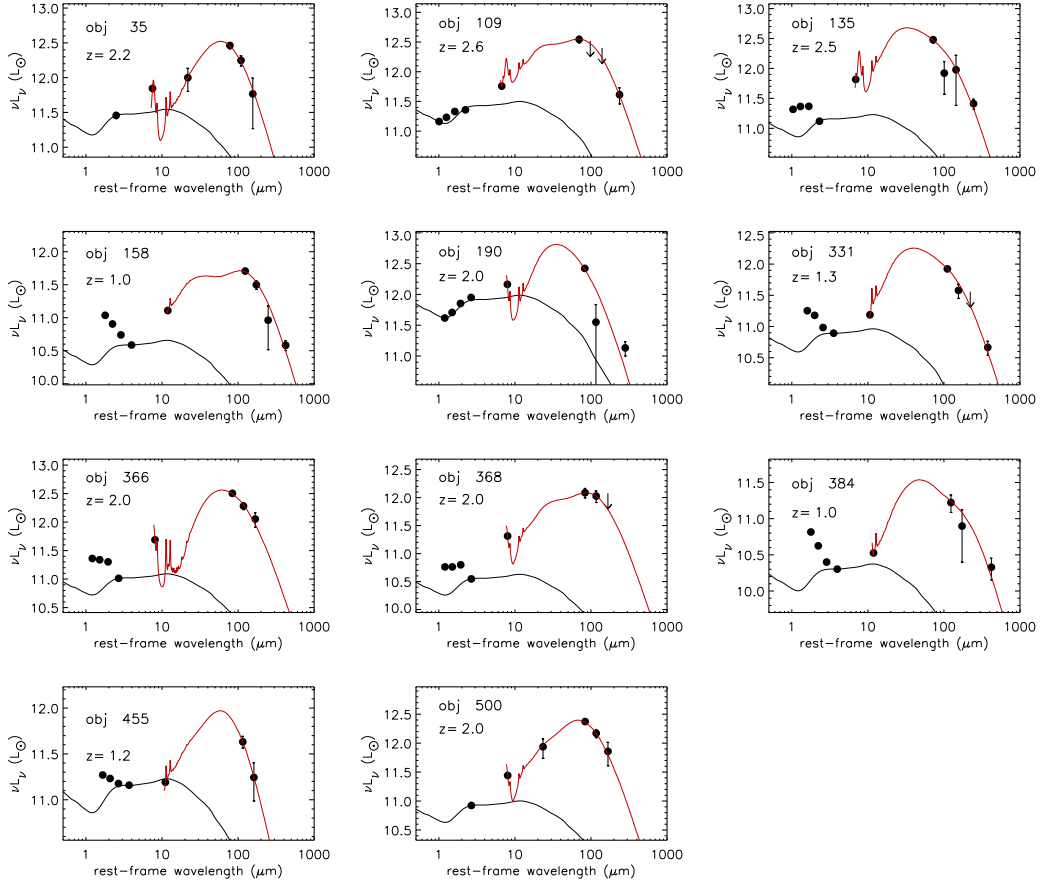


Figure S4: Infrared spectral energy distributions of 250 μm -detected AGN with $1 < z < 3$ and $10^{43} \text{ erg s}^{-1} < L_X < 10^{44} \text{ erg s}^{-1}$, based on SPIRE and *Spitzer* data. We included 850 μm and 1.3 mm photometry from ground-based telescopes where available^{41;42}. The black datapoints are the measured photometry, and the red lines show the star-forming model templates²⁶ which best fit the data at 24 μm and longward. The black lines show AGN templates⁴³, normalised in the mid-IR to estimate the AGN contribution²⁸. Each panel is labelled with the identity of the object in the X-ray catalogue¹².

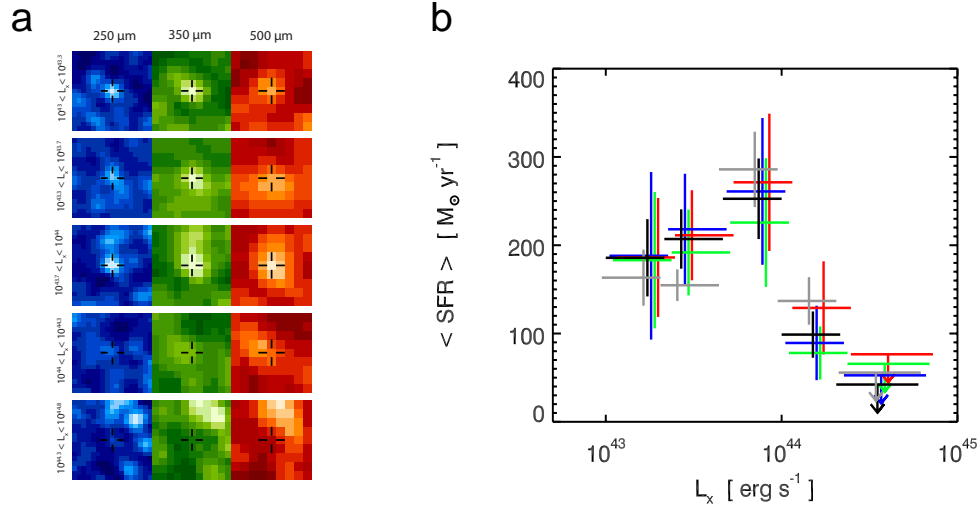


Figure S5: (a) Stacked 250, 350 and 500 μm SPIRE images of AGN in the five luminosity bins used for Fig. 2. The images are arranged in increasing wavelength from left to right and decreasing X-ray luminosity from bottom to top. (b) Star formation rates obtained from the stacked fluxes and median redshifts (grey) compared to the star formation rates obtained from stacking the luminosities as in Fig. 2 (black). The blue, green and red points show the star formation rates obtained in a similar fashion to the black points, but in these cases using only one of the SPIRE bands to determine the luminosities prior to averaging. Blue, green and red correspond to 250, 350 and 500 μm bands. The points have been offset slightly in the horizontal direction to aid clarity.

Fig. S5, and are consistent with each other as well as those shown in Fig. 2.

References

- [30] Barger A.J., et al., X-Ray, Optical, and Infrared Imaging and Spectral Properties of the 1 Ms Chandra Deep Field North Sources. *Astron. J.*, 124, 1839-1885 (2002)
- [31] Barger A.J., et al., Optical and Infrared Properties of the 2 Ms Chandra Deep Field North X-Ray Sources. *Astron. J.*, 126, 632-665 (2003)
- [32] Cohen J.G., et al., Redshift Clustering in the Hubble Deep Field. *Astrophys. J.*, 471, L5-L9 (1996)
- [33] Waddington I., et al., NICMOS Imaging of the Dusty Microjansky Radio Source VLA J123642+621331 at $z=4.424$. *Astrophys. J.*, 525, L77-L80 (1999)
- [34] Barger A.J., et al., Supermassive Black Hole Accretion History Inferred from a Large Sample of Chandra Hard X-Ray Sources. *Astron. J.*, 122, 2177-2189 (2001)
- [35] Wirth G.D., et al., The Team Keck Treasury Redshift Survey of the GOODS-North Field. *Astron. J.*, 127, 3121-3136 (2004)

- [36] Cowie L.L., et al., A Large Sample of Spectroscopic Redshifts in the ACS-GOODS Region of the Hubble Deep Field North. *Astron. J.*, 127, 3137-3145 (2004)
- [37] Donley J.L., Rieke G.H., Perez-Gonzalez P.G., Rigby J.R., Alonso-Herrero A., Spitzer Power-Law Active Galactic Nucleus Candidates in the Chandra Deep Field-North. *Astrophys. J.*, 660, 167-190 (2007)
- [38] Della Ceca R., et al., The cosmological properties of AGN in the XMM-Newton Hard Bright Survey. *Astron. Astrophys.*, 487, 119-130 (2008)
- [39] Lehmer B.D., et al., The Extended Chandra Deep Field-South Survey: Chandra Point-Source Catalogs. *Astrophys. J. Suppl.*, 161, 21-40 (2005)
- [40] Silverman J.D., et al., The Extended Chandra Deep Field-South Survey: Optical Spectroscopy of Faint X-ray Sources with the VLT and Keck. *Astrophys. J. Suppl.*, 191, 124-142 (2010)
- [41] Chapman S., Blain A.W., Smail I., Ivison R.J., A redshift survey of the submillimetre galaxy population. *Astrophys. J.*, 622, 772-796 (2005)
- [42] Tacconi L.J., et al., High-resolution millimetre imaging of submillimeter galaxies. *Astrophys. J.*, 640, 228-240
- [43] Elvis M., et al., Atlas of quasar energy distributions. *Astrophys. J. Suppl.*, 95, 1-68 (1994)